Detecting water leaks in underground pipelines by radar and dielectric analysis

Benhui Fan, Ao Wang, Jean-Marie Fleureau, Bruno Beaucamp, Vincent Guilbert, Cyril Ledun, Alain Sylvestre, Cyrille Fauchard

Detecting Water Leaks in Underground Pipelines by Radar and Dielectric Analysis

Benhui Fan[1]*, Ao Wang[1], Jean-Marie Fleureau[2], Bruno Beaucamp[1], Vincent Guilbert[1], Cyril Ledun[1], Alain Sylvestre[3], Cyrille Fauchard[1]*

[1]Cerema, Research Team ENDSUM, 10 chemin de la Poudrière, 76120, Le Grand-Quevilly, France

[2]Laboratoire de Mécanique Paris-Saclay, Université Paris-Saclay, CentraleSupélec, ENS Paris-Saclay, CNRS, 8-10 rue Joliot Curie, 91190 Gif-Sur-Yvette, France

[3]Université Grenoble Alpes, CNRS Grenoble INP G2Elab Grenoble 38000, France

Corresponding: benhui.fan@cerema.fr; cyrille.fauchard@cerema.fr

Abstract

Water leaks in underground pipelines not only lead to economic losses from wasted water but can also cause structural damage to urban infrastructure. In this study, we present a non-destructive radar-based detection for locating water leaks beneath the soil at various scales. First, as the radar detection relies on the dielectric contrast of soils with different saturation degrees, it is important to understand how the presence of water affects the dielectric permittivity and conductivity of unsaturated soils. To investigate this, the dielectric properties of three soil types: sand, loam, and a sand-loam-aggregate mixture, were analyzed by an open-ended probe to establish the relationship between the water saturation and the soil dielectric permittivity. Second, a stepped frequency radar (SFR) was employed in a controlled laboratory setting to monitor signal changes caused by water leaks in the three soil types. Finally, field tests were conducted at a site (8×5 m^2), where a ground-penetrating radar (GPR) was used to locate leaks in two plastic pipelines buried over 1 m deep, with varying leak speeds. Based on these multi-scale experimental results, we aim to demonstrate the potential application of radar-based measurement for water leak detection. Additionally, we discuss the signal variations caused by wet soils, soil deformation, and the accuracy of detection in different scenarios.

Key words: detecting water leaks, ground penetrating radar, dielectric properties, unsaturated soils,

Introduction

Water leaks from underground pipeline networks are among the major challenges faced by water management systems. With increasing pressures on water resources due to climate change, minimizing water waste caused by leakage is a critical strategy for enhancing water resilience [1, 2]. Additionally, prolonged water leaks that go unrepaired will bring the risk of underground hazards by weakening foundations and compromising the structural integrity of infrastructures [3, 4]. Hence, developing effective methods for detecting water leaks is essential for water management and sustainable urban development.

Several methods for detecting water leaks have been outlined in review articles [5-7]. Some of these methods, such as pressure and flow sensors or optical fibers, are already used in current practices. These techniques usually require sensors to be pre-installed, but unfortunately, many sites are not adequately equipped. Acoustic methods offer a non-destructive approach to detect leaks in water pipelines, but their effectiveness may be more or less influenced by environmental factors like urban noise and the material of the pipelines. Considering the practicality and detection accuracy, radar-based methods present a promising and complementary alternative to existing techniques.

Radar measurements are based on the propagation of electromagnetic (EM) waves, and the detection principle depends on the dielectric contrast between water (with a dielectric constant of 78-80 [8]) and the surrounding soils. When soil is dry, its dielectric constant is relatively low (often less than 5, deduced by the relation of the dielectric permittivity and the specific density (2.65 g/cm^3), proposed by Campbell [9]). However, when soil becomes wet, its dielectric properties and conductivity increase to varying degrees, depending on soil's characteristics, such as clay content, saturation degree (porosity and water content), and mineralogical composition, etc. [10-12]. This change in dielectric properties creates contrasts in radargrams that makes radar detection possible [13,14]. Nevertheless, a significant challenge stems from the heterogeneous nature of unsaturated soil of various scales and types, especially at different depths, along with the complexity of unknown underground structures. These factors can greatly influence EM waves propagation and consequently create the anomalies in a radargram. Differentiating anomalies caused by water leaks from those resulting from wet soil around pipelines or other subsurface features remains a critical difficulty in this field. In addition, there is a trade-off between radar detection depth and resolution, which depends on the applied wavelength and central frequency of the EM waves. Hence, finding the optimal balance between these parameters is crucial for effective detection.

Many studies have focused on classifying anomalies in radargrams by simulation [15-17]. However, some of these studies rely on datasets that are not derived from multi-scale and multi-soil experimental tests. Specially, the dielectric measurements of unsaturated soils are often less investigated, which makes the simulation of the radargrams less representative. Moreover, the experimental scenarios tend to be more complex, involving large-scale sites, diverse underground layers with varying soil characteristics, and complex leakage processes, etc., where simulations often have difficulty to fully replicate. In addition to simulation-based research, there are reports that discuss the practical application of radar for detecting water leaks [18-20]. These studies were typically constrained to laboratory scales and most of them often used sand as the primary soil type. Although they offer valuable insights into EM wave propagation in unsaturated soils, their findings may not be migrated to the behavior of other soil types. Furthermore, a few reports can also be found to present radar-based water leak detection in real environments [21-25]. These studies are helpful in demonstrating the applications of radar, but some of them do not adequately address the evolution of radar signals caused by water leaks. Therefore, in this study, we aim to

demonstrate the application of radar for detecting water leaks from pipelines across various soil types and test scales.

The study is organized into three parts: (i) Material Analysis: we characterize the dielectric properties of three unsaturated soils (sand, loam, and a sand-loam-aggregate mixture) with controlled saturations by an open-ended dielectric probe. (ii) Physical Model Analysis: We use the three soils to create physical models and observe the evolution of EM signals caused by water leakage on an intermediate scale, by a stepped-frequency radar (SFR). This includes monitoring the movement of wet soils in the physical models, the deformation of surface soils due to liquefaction, and estimating soil saturation during the leakage process. (iii) Site Test: We build a full-scaled site involving two pipelines buried more than 1 meter deep in loamy sand, where we observe the evolution of radargram anomalies caused by water leaks at different leakage speeds by a ground penetrating radar (GPR). In this section, we discuss the relationship between detection accuracy and leakage duration/speed. Additionally, we examine structural damage, such as sinkholes, caused by long-term underground water leaks.

Dielectric studies of three soils

I. Preparation of unsaturated soils with controllable saturation degrees

Three types of soils were used in this study: masonry sand, loam, and a mixture of sand, loam, and siliceous aggregates sourced from the Criquebeuf quarry (Seine-Maritime, France), as shown in the photo in Figure 1(a). These will be referred to as "sand," "loam," and "Criquebeuf," respectively. The plasticity of loam and Criquebeuf was characterized by methylene blue test. For both soils, the blue value (VBS) was less than 2.5, classifying them as "sandy clay, low plasticity" [26].

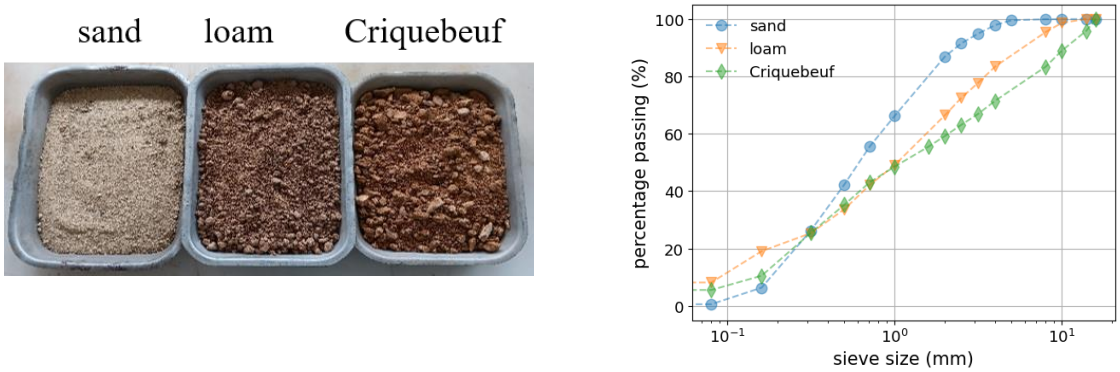

(a) (b)

Figure 1 (a) Photo of the three soils: sand, loam and Criquebeuf; (b) Grain size distribution of sand, loam and Criquebeuf.

To analyze the propagation of EM waves in soils, both with and without water leaks, it is essential to know the dielectric properties of the soils as a function of their water content. This is because the velocity of EM waves in microwave domain is typically determined by the dielectric permittivity of the medium, while the attenuation of EM waves is governed by its conductivity. Since soils are porous materials, both water volumetric fraction and porosity simultaneously influence the dielectric permittivity. Therefore, we will use an open-ended probe to measure the dielectric properties of soils with controlled moisture and compaction levels.

To prepare the samples with controllable saturation degree, grains larger than 20 mm were removed for two reasons: (1) aggregate's size range for the dielectric measurement by open-ended probe and (2)

relatively homogeneous compaction by press machine. The grain size distribution of the three soils used for the dielectric tests is shown in Figure 1(b). The soils were first dried in an oven at 105 °C for 24 h. Then, the soils were well mixed with the calculated amount of water. Prior to performing the dielectric measurements, the soils were left for two weeks in a sealed plastic bag to allow the water distribution to homogenize.

To achieve a sample with well-controlled water saturation, we used a press (hydraulic compression, MTS) to compact the soil in a PVC mold (the inner diameter Φ = 155 mm). The test setup is shown in Figure 2(a). By controlling the piston settlement (H^i) in the mold after each compression (e.g., 1 cm, 2 cm, 3 cm, up to the maximum force of the machine, 60 kN), the humid density of the soil (ρ_h^i) can be calculated from its initial weight (m = 4 kg) and the actual volume in the mold (Eq-1):

$$\rho_h^i = \frac{m}{\Phi(H_{mold} - T_{piston} - H^i)} \qquad \text{(Eq-1)}$$

where the superscript i denotes different compression stages; H_{mold} and T_{piston} represent the initial height of the mold (174.5 mm) and the thickness of the piston (25.5 mm), respectively. After the tests, soil samples were taken from both the lower and upper layers of the mold, weighted and then heated in an oven at 105 °C for 24 h. This allowed us to calculate the average gravimetric water content (w) (Eq-2) and dry density of the soil (ρ_d^i) (Eq-3):

$$w = \frac{m_{water}}{m_{soil\_dry}} \qquad \text{(Eq-2)}$$

$$\rho_d^i = \frac{\rho_h^i}{1+w} \qquad \text{(Eq-3)}$$

The volumetric water content (θ^i), porosity (n^i), and degree of saturation (S_r^i) of the soil after each compression were calculated using Eq-4a, Eq-4b, and Eq-4c:

$$\theta^i = \rho_h^i * \frac{w}{1+w} \qquad \text{(Eq-4a)}$$

$$n^i = 1 - \frac{\rho_h^i}{(1+w)*\rho_s} \qquad \text{(Eq-4b)}$$

$$S_r{}^i = \frac{\theta^i}{n^i} \qquad \text{(Eq-4c)}$$

Where ρ_s is the specific density of soil, 2.65 g/cm^3 is used in the calculation based on the values in reference [10-12].

The compactness of the soil depends on its plastic properties. Therefore, it is important to verify the ρ_d^i and w of the tested samples to ensure that the degree of saturation (S_r^i) of all samples remains less than 1, as shown in Figure 2(b).

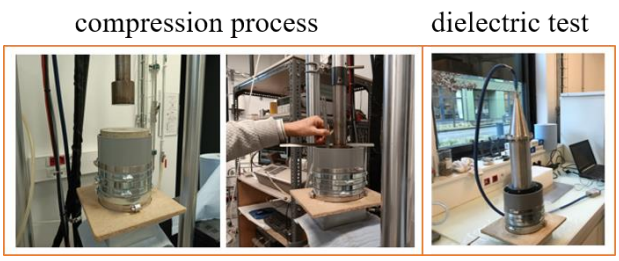

(a)

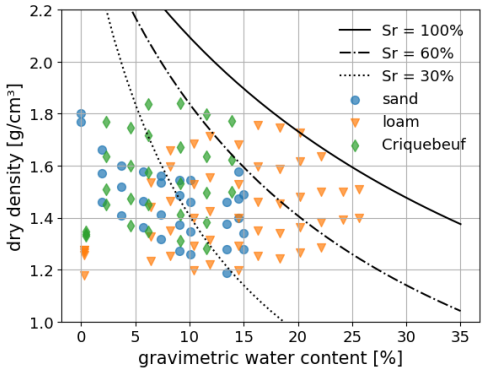

(b)

Figure 2 (a) Control of the different piston depressions in the mold by press and dielectric test using an open-ended probe. (b) Dry density (ρ_d) and gravimetric water content (w) for the three soils after each compression.

II Dielectric analysis and model establishment

The open-ended probe used in this test is shown in the right part of Figure 2(a). The principle behind this test is detailed in our previous works and other references [27-29]. The probe has a characteristic impedance (Z_0) of 50 Ω. Frequency-dependent relative dielectric permittivities are calculated based on complex reflection coefficients (S_{11}) using capacitance way. The EM source was generated by a reflectometer (R60, Copper Mountain Technologies) and the frequency range was from 50 MHz to 1.6 GHz. The calibration was performed by the automatic calibration module (ACM2520, Copper Mountain). The highest frequency used for a measurement ($f_{cut\ off}$) is determined by two factors: the dielectric constant of the sample and the probe's geometry (Eq-5) [30]:

$$f_{cut-off}(MHz) = \frac{20}{(b-a)\sqrt{\varepsilon_r'}} \qquad \text{(Eq-5)}$$

where a (16.1 mm) and b (37.5 mm) are the inner and outer radii of the probe, respectively, and ε'_r is the real relative dielectric permittivity of the medium being tested.

Because of the heterogeneity of the soil types (sand, loam, and aggregates in Criquebeuf), a probe with a large aperture was necessary. Three measurements were taken for each sample, and an average value was calculated. When the soil is not dry, ε'_r can be in a large range. An example of loam with four saturation degrees is shown in Figure 3(a), illustrating the measured frequency dependent complex dielectric permittivity. The obtained permittivity is stable in the tested frequency range. As the saturation degree increases with successive compressions, the dielectric permittivity also rises. Considering the geometry of the probe and the tested dielectric range of the soils, the highest frequency was cut at 450 MHz, resulting in an effective range of 50 MHz to 450 MHz presented in Figure 3(a).

The dielectric constant measured at 250 MHz is used to establish the relationship between saturation and dielectric permittivity in the following part. It is important to note that 250 MHz is lower than the radar frequency used in this work (GHz). To estimate the instantaneous dielectric constant (ε_∞), dielectric relaxation models such as Debye, Havriliak-Negami (HN), and Jonscher have often been used to fit the frequency-dependent dielectric permittivity in many studies [31]. However, in our case, the relatively narrow frequency range (50 MHz to 450 MHz) limits the applicability of these models. Moreover, as shown in the dielectric dispersion spectra reported by A. Revil [32] in Figure 3(b), the

frequency-dependent dielectric permittivity is influenced by three types of polarization mechanisms: double-layer (α) polarization (10^{-3}–10^{4} Hz), Maxwell-Wagner (β) polarization (10^{3}–10^{9} Hz), and dipolar (γ) polarization (10^{9}–10^{11} Hz). The dielectric permittivity measured in this frequency range (50 MHz-450 MHz) is predominantly influenced by β polarization, while the radar frequency domain (GHz) is affected by both β and γ polarizations. However, the dispersion of dielectric permittivity significantly diminishes within the frequency range of 10^{8} Hz to 10^{10} Hz. Therefore, we believe that the dielectric permittivity measured at 250 MHz can reasonably represent the behavior of EM wave propagation in the radar frequency domain. Consequently, we use the permittivity measured at 250 MHz to compare the dielectric behavior of the three soils under varying saturation degrees.

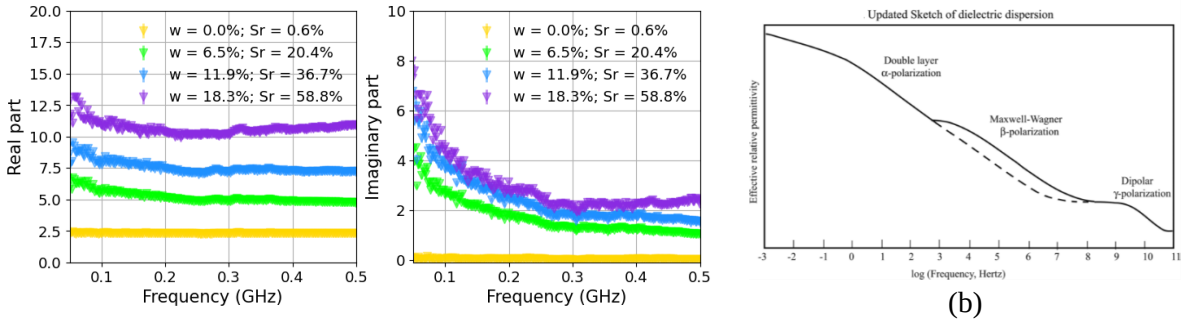

(a) (b)

Figure 3 (a) Frequency-dependent dielectric permittivity of loam with four saturation degrees, showing the real part, ε'_r (left) and imaginary part, ε''_r (right). (b) Illustration of the three types of polarization mechanisms as proposed by A. Revil. [32]

As mentioned earlier, the dielectric permittivity of soils generally depends on fine content, water content, porosity, and mineralogical composition, etc.. In this study, we do not focus on the influence of mineralogical composition, since the soils used originate from the same region. We mainly examine the effects of water content and porosity.

Numerous models have explored the relationship between water content and soil dielectric properties and most rely on volumetric water content (θ), such as Topp model [33] and models based on mixing laws like CRIM [34]. However, using models based on θ presents an inconvenience for practical applications: most geotechnical soil data are expressed in terms of gravimetric water content (w) and void ratios rather than θ. Obtaining θ from such data is not straightforward. Alternatively, using the degree of saturation (S_r), defined as the ratio of θ to porosity (n, see Eq-3c), can offer a more practical approach. This makes it easier to integrate data from dielectric and mechanical studies. Therefore, we present models relating S_r to the dielectric properties measured at 250 MHz in Figure 4(a) and (b).

As shown in Figure 4(a), the real permittivity (ε_r') values measured with the open-ended probe exhibit a linear dependence on saturation degree for all three soil types.

For conductivity (σ), we first explain its calculation from dielectric properties. σ can be determined by the imaginary part of the complex relative dielectric permittivity (ε_r''), which corresponds to EM energy loss, as expressed in Eq-6:

$$\sigma = 2\pi f \varepsilon_0 \varepsilon_r^{''} \qquad \text{(Eq-6)}$$

Where f is the frequency (250 MHz) and ε_0 is the permittivity of free space (8.856×10^{-12} F/m).

The effects of water on soil conductivity are complex, as soils contain ions that dissolve in water, forming a pore fluid with conductivity higher than that of fresh water. If we used the conductivity of fresh water ($1.5 – 5 \times 10^{-4}$ S/m) [8] and apply mixing laws, the calculated σ would deviate from the experimental results. To address this issue, A. Revil proposed a method [32] (Eq-7) for estimating soil conductivity based on the Archie model:

$$\sigma \approx \theta^m \sigma_w + \theta^{m-1} \sigma_s \qquad \text{(Eq-7)}$$

Where σ_w and σ_s represent the conductivity of the pore fluid and the grains, respectively, and m is an empirical exponent. The conductivity of the pore fluid (σ_w) can be estimated by another empirical model proposed by N. Wagner et al. [11], which is based on n and θ, as shown in Eq-8.

$$log_{10}\big(\sigma_w(\theta, n)\big) = log_{10} A + Bn + C\frac{\theta}{n} \qquad \text{(Eq-8)}$$

By combining Eq-7 and Eq-8, we can develop a model to describe our test results. We used 44×10^{-4} S/m as the value for σ_s [32]. A, B, and C are fitted by the Gauss-Newton algorithm in the curve fit function of the Python Scipy Optimize package. Their values for the three soils are provided in Table 1. As shown in Figure 4(b), the models effectively relate σ and S_r for these three soils.

Furthermore, as shown in Figure 4, loam exhibits the highest values for ε_r' and σ, while sand shows the lowest. The dielectric properties of Criquebeuf are intermediate: for ε_r', Criquebeuf is closer to sand, but for σ, it is closer to loam. The differences in dielectric properties among the three soils are possibly associated to the geometry of the grains. In unsaturated soils, the size and shape of the grains play an important role [8, 10]. In our measurements, successive compressions were applied to a sample with a given gravimetric water content to achieve varying densities. This dynamic process affects the distribution of pore water within the soil voids. In the case of sand, the grain shape is more particle-like with a relatively homogeneous size distribution. This geometry facilitates the drainage of water through the particles. In the case of loam, the content of fines (grains smaller than 80-100 µm) is higher than that in sand, as shown in Figure 1(b). The fines have a large specific surface area, which allows the soil to swell after two weeks of homogenization. As a result, at the same saturation, the water network in loam is more easily interconnected than in sand, leading to a higher dielectric permittivity and conductivity in loam compared to sand. Criquebeuf, being a mixture of loam, sand, and aggregates, has a large distribution of grain size, which brings its real permittivity closer to that of sand. However, the heterogeneous structure of Criquebeuf can result in a more complex ion content, making its imaginary dielectric permittivity (or conductivity) more similar to that of loam. We did not characterize the mineralogical properties, polycrystalline structures, and micro-morphology of these soils. Thus, this is an assumption. We believe this part of the study should need further analysis in future, especially for the discussion at the low frequency (0.1 Hz to 1M Hz) measured by impedance spectroscopy.

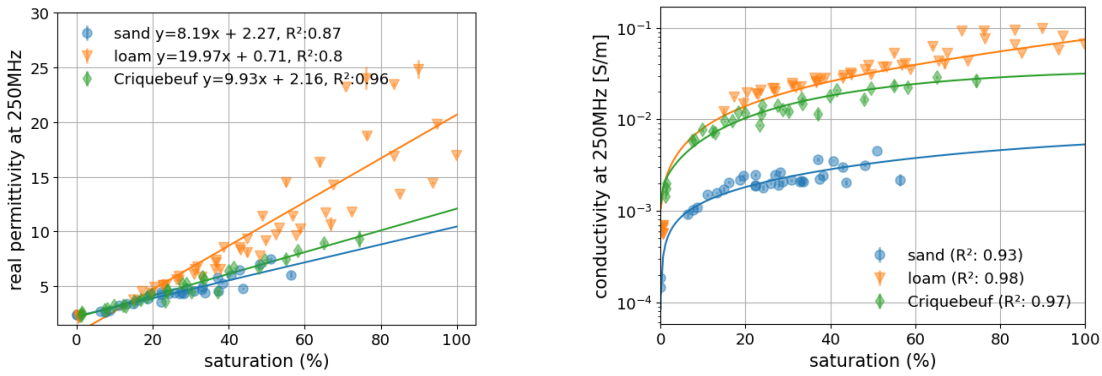

(a) (b)

Figure 4 (a) Relationship between saturation (S_r) and real dielectric permittivity (ε_r') measured at 250 MHz; (b) Relationship between saturation (S_r) and conductivity (σ) at 250 MHz.

Table 1 Parameters relating electrical conductivity (σ) at 250 MHz to saturation (S_r)

soil	m	A	B	C
sand	1.47	0.09	-1.79	-0.18
loam	1.19	0.05	0.91	0.45
Criquebeuf	1.17	0.58	-1.35	-0.29

Analysis the propagation of EM waves by physical models in laboratory

I. Experimental setup description

A physical model was prepared in a polyvinyl chloride (PVC) box (80 × 60 × 52 cm³) in the laboratory to observe water leakage by a stepped frequency radar (SFR). The setup, shown in Figure 5, consisted of two layers. The first layer, approximately 7.5 cm thick, was composed of sand and supported a PVC tube. The second layer, about 25 cm thick, covered the tube and consisted of either sand, loam, or Criquebeuf, as illustrated on the left side of Figure 5. To simulate a homogeneous leakage, two PVC tube sections (Φ_{ext} = 32 mm, Φ_{int} = 28 mm) were connected by a third PVC tube with a slightly larger diameter (Φ_{ext} = 40 mm, Φ_{int} = 36 mm). Due to the limited size of the box, achieving reproducible compaction of the soil layers by machinery was difficult, thus the materials of both layers were not compacted. In addition, a density gradient in the second layer caused by the accumulation of overlying soil may have developed during the preparation. This density gradient cannot be avoided, especially in the cases of loam and Criquebeuf. We will discuss it in the B-scan results.

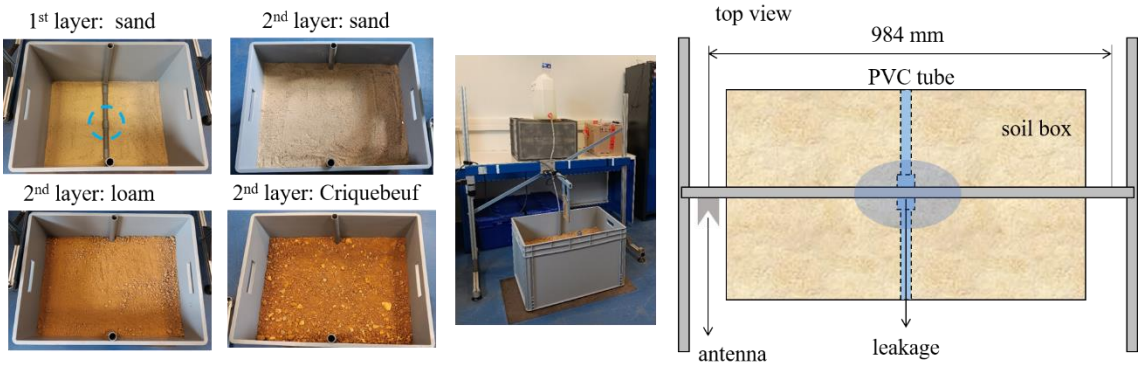

Figure 5 Model and setup used to observe water leakage with a stepped frequency radar (SFR).

The antenna used in the test was an exponentially tapered slot antenna (ESTA), also known as a Vivaldi antenna. The EM generator was a reflectometer (R60, Copper Mountain Technologies), operating within the frequency range from 1.4 GHz to 6 GHz. The calibration was performed using its automatic module (ACM2520). The measurement length was 984 mm, with a 5 mm interval, which sufficiently covered the entire length of the box (800 mm), as shown in the right part of Figure 5. To track the evolution of the signals, radargrams (B-scans) were recorded every 3 min based on the speed of scanning and the duration of calibrating. As the setup was stable where the antenna and cables were well fixed, during the test we did not observe the noise or the baseline drift corresponding to the antenna or its movement. The EM acquisition was stopped once the water sufficiently wetted the surface of the second soil layer.

II. EM wave analysis by stepped-frequency radar

In Figure 6, we present three A-scan signals: (i) a raw A-scan from the antenna to air, (ii) a raw A-scan from the antenna to the ground at the center of the tested system, and (iii) the processed signal obtained by applying a treatment to the second raw signal. The treatment involves two steps: first, removing the antenna response, and second, multiplying by a gain function [35]. In this gain function (Eq-9), a is a linear factor set to 1, v is the velocity depending on the dielectric permittivity of the tested medium. b is the exponent, which varies from 10 to 25 in this work.

$$g(t) = (1 + A * t) * e^{B*t} \qquad \text{(Eq-9a)}$$

$$A = \frac{a}{pulse\ width} \qquad \text{(Eq-9b)}$$

$$B = \frac{b*v}{8.69} \qquad \text{(Eq-9c)}$$

Using the gain function, we can amplify the signals after 5 ns. This time domain corresponds to the interface between the first and second soil layers in our system when the soil is dry. As shown in Figure 6, a change in the signals occurs between 6.5 ns and 7 ns in the raw signals (highlighted by the blue dashed lines) for the sand and Criquebeuf cases. This change is attributed to the iron plate beneath the PVC box. However, in the loam case, this signal change is not as apparent. Despite this, we can still identify the iron plate's influence in the processed signal in the loam case.

We also present a B-scan, which is an assembly of A-scans across the entire tested distance for the sand case before the leakage, as shown in Figure 6(d). To facilitate the interpretation of the B-scan, we used photogrammetry to scan the sand case, and created a 3D model. This model was then combined with the B-scan, allowing us to better display our system. In the B-scan, several environmental effects are observed: (1) Two hyperbolas around 2 ns – these are associated with the left and right edges of the PVC box. (2) A line at approximately 4.5 ns – This feature corresponds to the aluminum (Al) motor support in the setup. (3) Hyperbolas at about 5.5 ns – These are caused by the two vertical aluminum supports. (4) A line at 6.5 ns – This reflection is linked to the bottom of the box resting on the iron plate. (5) Signals below 7 ns – These represent reflections from the foundation of the laboratory. The signals associated with the two soil layers are found between 3 ns and 6.5 ns before the leakage. Moreover, a hyperbola can be seen before 6 ns between 200 mm and 600 mm on the position axis (x), which corresponds to the trace of the PVC tube.

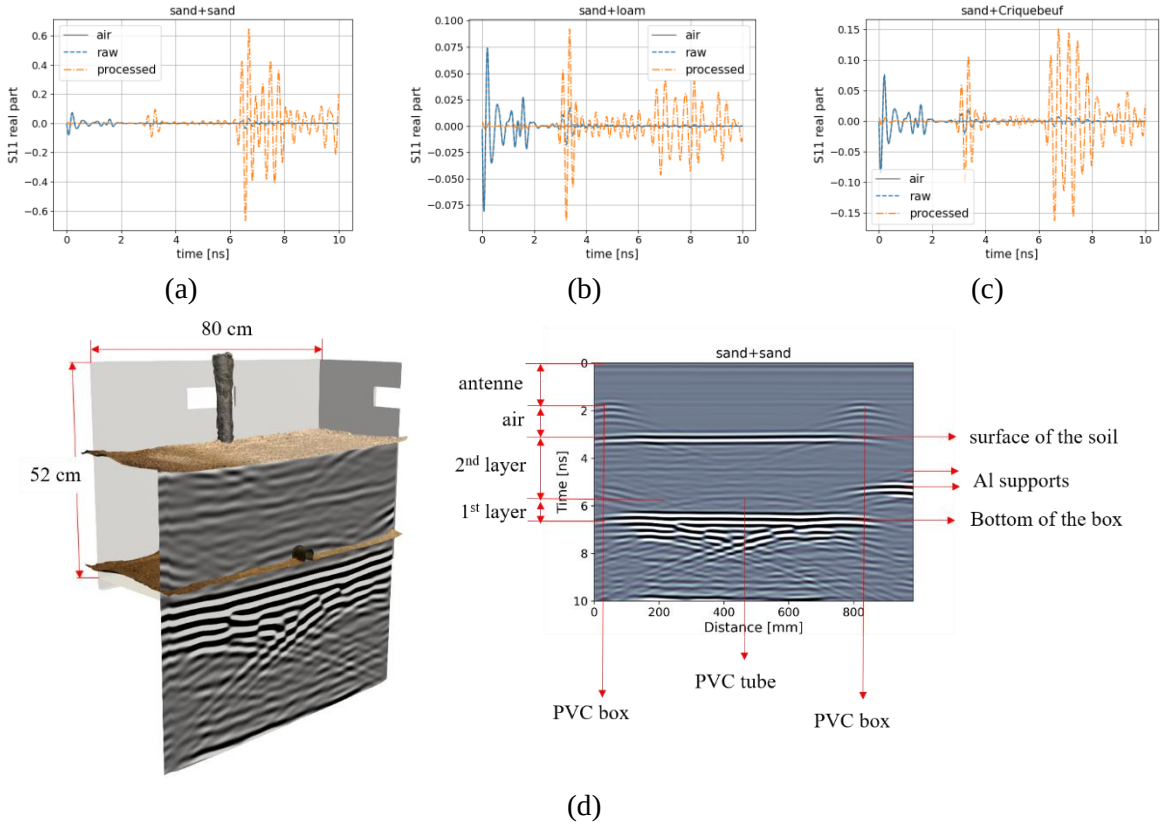

Figure 6 A-scans of the tested signals propagated in air, and in the soil, before and after processing by the gain function: (a) Sand, (b) Loam, and (c) Criquebeuf; (d) Illustration of the combination of B-scan and 3D model constructed by photogrammetry.

A 10 l bottle was used to supply water to the system. To maintain a relatively constant flow rate during the test, the water level in the bottle was kept above a minimum threshold. To estimate the flow rate, each time the water reached the minimum level, 1.5 l of water was added, and the time taken for the water to reach the minimum level again was recorded. By measuring the average time to consume 1.5 l of water at least ten times, an estimate of the flow rate in the tested system could be obtained. The average flow rates for the three cases (sand, loam, and Criquebeuf) are provided in Table 2. Additionally, the initial gravimetric water content (w) of the second layer before the leak is also listed in Table 2.

Table 2 Water flow rate in the system and initial gravimetric water content of the soils before leakage

	sand	**loam**	**Criquebeuf**
water flow (l/min)	0.18 ± 0.02	0.13 ± 0.03	0.26 ± 0.02
initial gravimetric water content	0.1 %	3.7 %	1.1 %

We selected several B-scans that illustrate the changes in the signals during the leakage process, as shown in Figure 7. The number in the upper left corner of each B-scan corresponds to the duration of the leakage, with "00" indicating the B-scan before the leakage begins. In the #00 B-scans, the bottom line is visible in the B-scans for all three cases. However, only in the sand case can we clearly observe the hyperbola associated with the PVC tube, due to the homogeneous structure of the sand. In the loam and Criquebeuf cases, the hyperbola is masked by the heterogeneous structure, and the density gradient of the soil. This is one reason why we observe a multilayered structure in the B-scans of loam and Criquebeuf, which possibly results from the non-uniform compaction using manual filling.

After water leakage occurs, the signal from the bottom becomes less visible, shifting from 6-7 ns to 7-8 ns due to the reduced velocity of the EM wave in the wet soil with higher dielectric permittivity. As the leakage continues, the signal related to the bottom eventually disappears. Simultaneously, a trace indicating the front of the wet soil starts to appear, as shown by the yellow flashes. In the sand case, this front is visible from B-scan #03 to #28 and progressively moves toward the surface. In the loam and Criquebeuf cases, the front is mixed with the heterogeneous structure of the soil and becomes noticeable later in the B-scans: from #16 to #26 for loam and from #20 to #28 for Criquebeuf. Once the wet soil front reaches the surface, it merges with the surface soil signal, becoming less distinct, as seen in the final B-scan for all three cases in Figure 7.

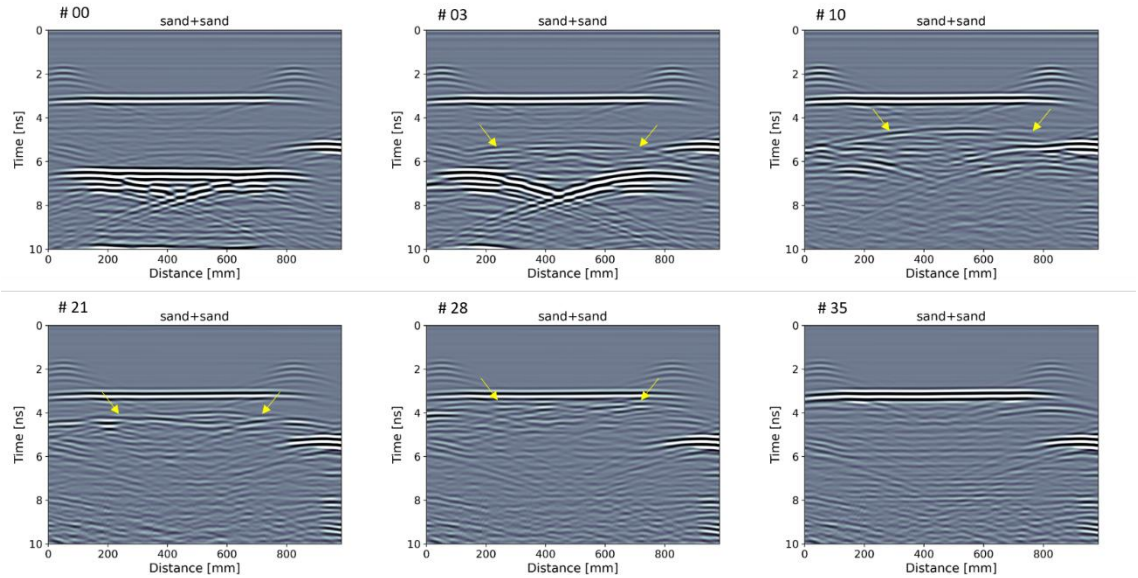

(a)

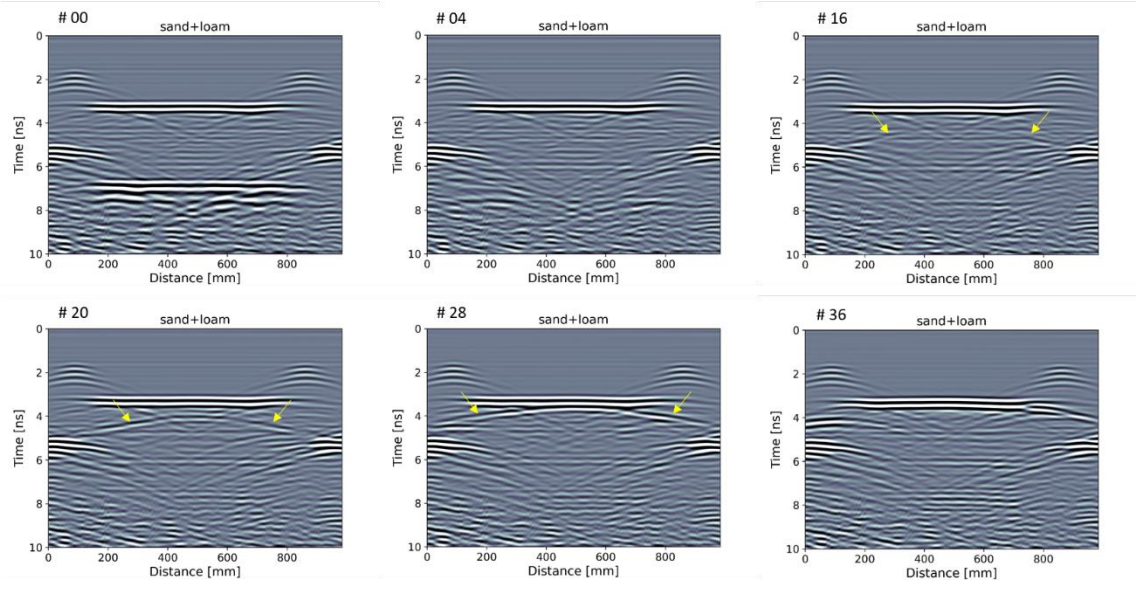

(b)

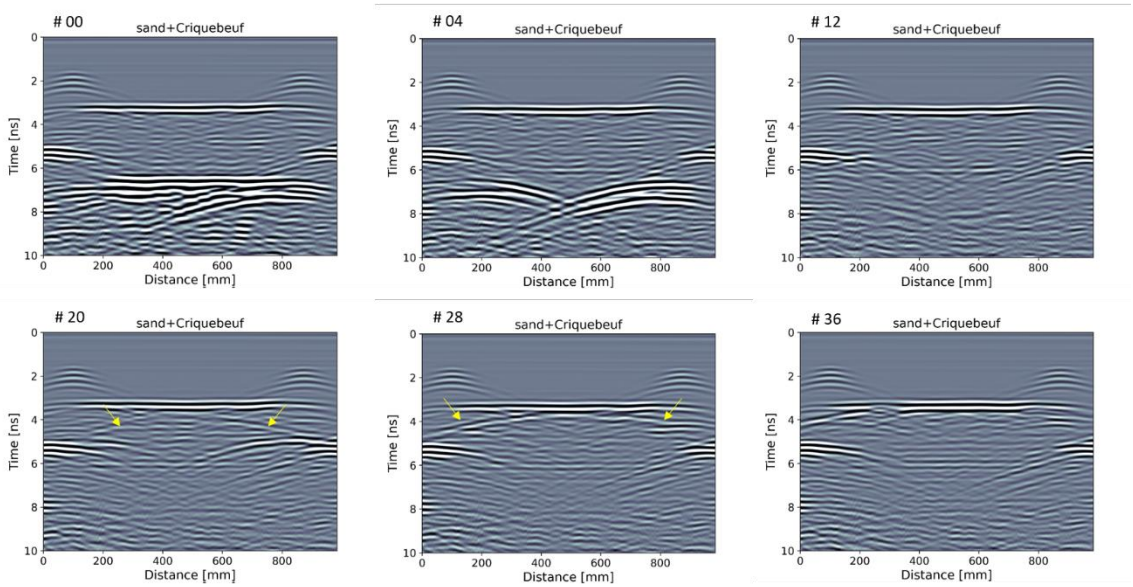

(c)

Figure 7 Evolution of the signals in Bscans during the leakage (a) for sand, (b) for loam and (c) for Criquebeuf. The yellow arrows present the front of the wet soil.

By examining the A-scans at the leakage point in the center of the box for all three cases, we can discover more information related to the geometric changes caused by the leakage. As shown in Table 2, the flow rate in the loam case is the slowest, while the Criquebeuf case exhibits the fastest flow rate. This difference in flow rates results in a varying number of measurements: 70 measurements for the sand case, 80 for the loam case, and 40 for the Criquebeuf case. To facilitate comparison of the signals under similar water volumes in the box, we selected A-scans at regular intervals: for the sand and loam cases, we chose the 1st, 3rd, 5th, and so on, totaling 35 A-scans for sand and 40 A-scans for loam. In the Criquebeuf case, all 40 A-scans were used for the analysis.

Since the waveform of the signals during the measurements, both with and without leakage, does not change much, we can use a "wiggle" presentation—commonly used in the seismic field—to illustrate the amplitude changes in the signals over time during the water leakage process. The wiggle plots for the three cases are shown in Figure 8. Each curve represents the difference (Δ) between two adjacent A-scans, as described in Eq-10:

$$\Delta = A\_scan^{i} - A\_scan^{i-1} \qquad \text{(Eq-10)}$$

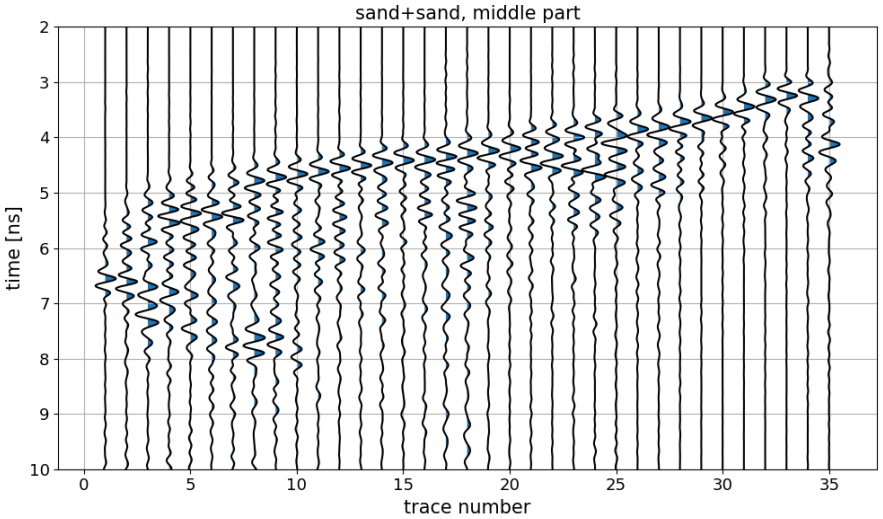
sand+sand, middle part
time [ns]
trace number

(a)

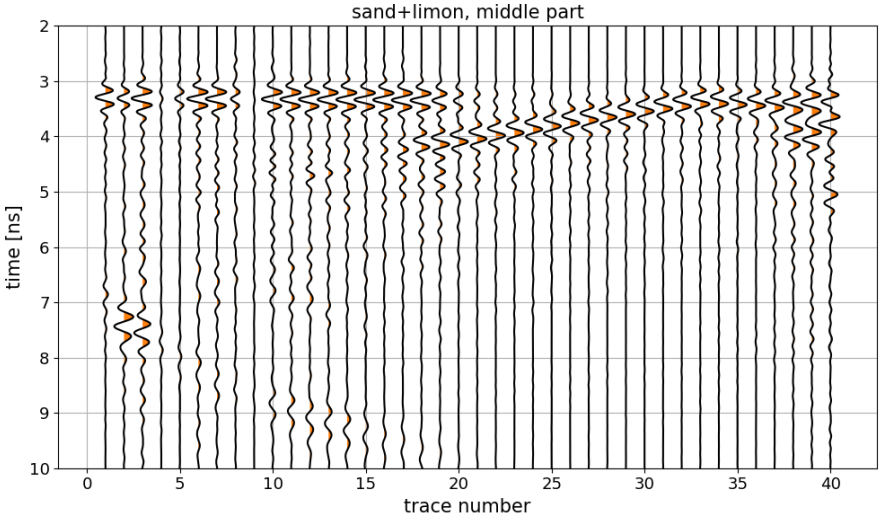
sand+limon, middle part
time [ns]
trace number

(b)

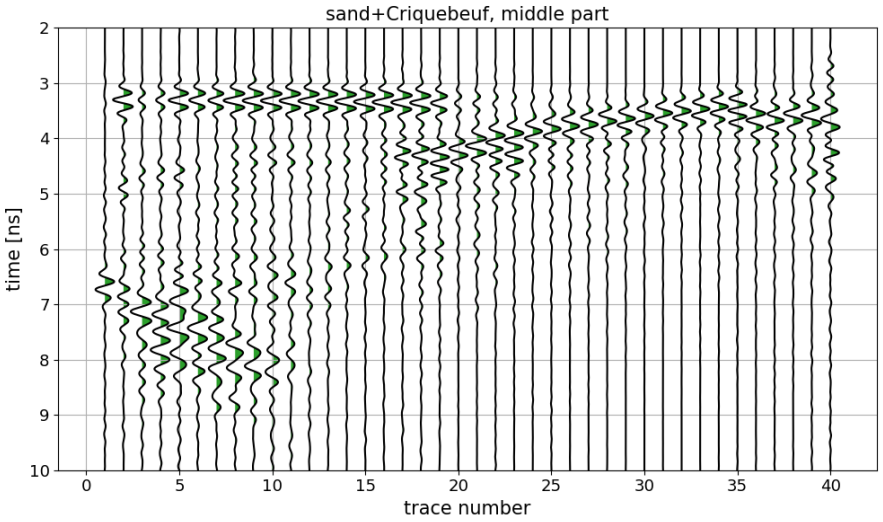
sand+Criquebeuf, middle part
time [ns]
trace number

(c)

Figure 8 Difference (Δ) between two adjacent A-scan^{i} and A-scan^{i-1} for the cases of sand (a), loam (b) and Criquebeuf (c).

In the case of the sand, we observe that initially, the blue peaks associated with the leakage are located at 6.5 ns. Over time, these peaks shift downward to 8 ns, and then gradually rise back up to 3 ns. This process is associated to the movement of the wet soil front in the box, as explained earlier. At the beginning, the water flows and effectively wets the first layer. Once the bottom layer is fully saturated, the water begins to rise and gradually wets the sand in the second layer, eventually reaching the surface.

In the case of the loam, the movement of the wet soil, marked in orange, differs a bit from that observed in sand. Initially, peaks are visible at 6-7 ns in the first two traces, corresponding to the wet soil front in the first layer. However, these peaks become less visible as the leakage progresses and reappear only after the 20th trace. This behavior is due to the heterogeneous structure and relatively high conductivity of wet loam, as mentioned earlier. Unlike the sand case, in loam, another distinct movement occurs at 3.5 ns, particularly in the first 15 traces. This movement is related to the travel time between the antenna and the surface of the loam. After around 25 traces, this change begins to merge with the wet soil front. Thus, for loam, we can conclude that: (i) the movement of the wet soil front is less distinct in the early stages; and (ii) the travel time between the antenna and the soil surface changes during the leakage process.

In the case of the Criquebeuf, we can observe both the movement of the wet soil front, though it is less distinct in the B-scans, and the changes in travel time between the antenna and the surface of Criquebeuf during the leakage process.

The variation in travel time between the antenna and the soil surface infers change in this distance, as the speed of the EM wave in air remains constant. This variation can be associated with potential deformation of the soil surface caused by the leakage. To estimate this deformation, we calculated the shift in the peak of the absolute value of the signal ($|S_{11}|$) in the time domain, as shown in Figure 9 (a) to (c). By calculating the difference between the peak times of the antenna and those of the soil surface, we obtain the round-trip time (Δt^{i}) of the EM wave. The distance for this trip can be calculated by Eq-11a, where the signal speed in air (c) is 3×10^{8}m/s. The change in distance (Δd^{i}) can then be determined by subtracting each d^{i} from the initial d^{0}, before the water leakage, as shown in Eq-11b:

$$d^{i} = c\frac{\Delta t^{i}}{2} \qquad \text{(Eq-11a)}$$

$$\Delta d^{i} = d^{i} - d^{0} \qquad \text{(Eq-11b)}$$

The results for the three cases are shown in Figure 9(d). Before the 25th trace, when the font of the wet soil has not yet merged with the portion of the signal travel time in air, the calculated results remain stable. In the sand case, the distance between the antenna and the sand does not show significant changes. However, in the loam and Criquebeuf cases, the distance continues to increase, suggesting a deconsolidation of the soil caused by the liquefaction occurring beneath the surface.

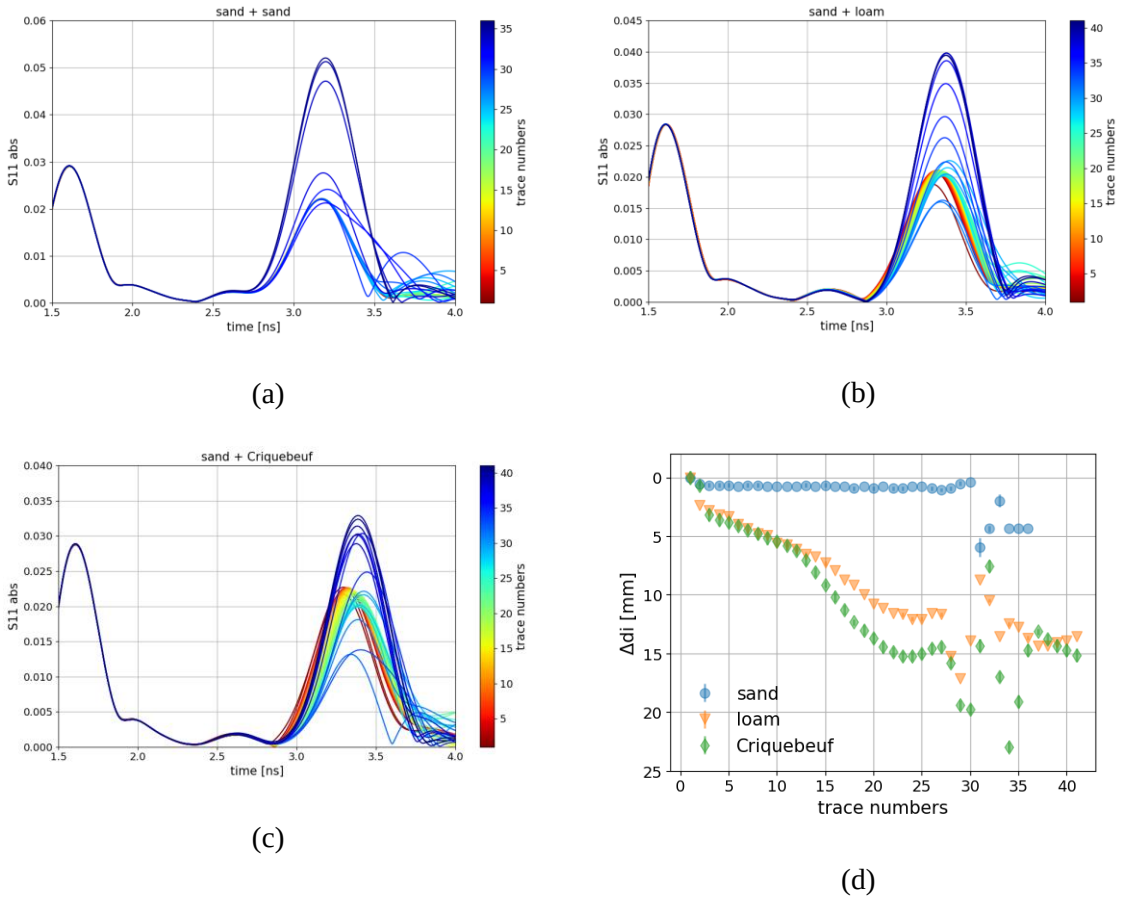

Figure 9 Shifts of the peaks of the$|S_{11}|$ in the time domain: (a) sand, (b) loam, and (c) Criquebeuf; (d) change in the distance between the antenna and the soil surface.

Additionally, the amplitudes of $|S_{11}|$ at the soil surface can be used to estimate the reflection coefficient (R_s) [36], as shown in Eq-12a. Here, A_{soil} represents the amplitude of $|S_{11}|$ observed at the soil surface during the leakage (i.e., the peaks occurring after 3 ns in Figures 9(a) to (c)), while A_{met} corresponds to the amplitude of total reflection from the metal.

$$R_s = \frac{A_{soil}}{A_{met}} \qquad \text{(Eq-12-a)}$$

$$\varepsilon_r' = \left(\frac{1+R_s}{1-R_s}\right)^2 \qquad \text{(Eq-12-b)}$$

Based on R_s, the surface dielectric constant of the soil during the leakage can be estimated using Eq-12b, as shown in Figure 10(a). By combining this with the model of real dielectric permittivity and saturation presented in Figure 4(a), we can estimate the evolution of the surface soil properties in the system, as illustrated in Figure 10(b).

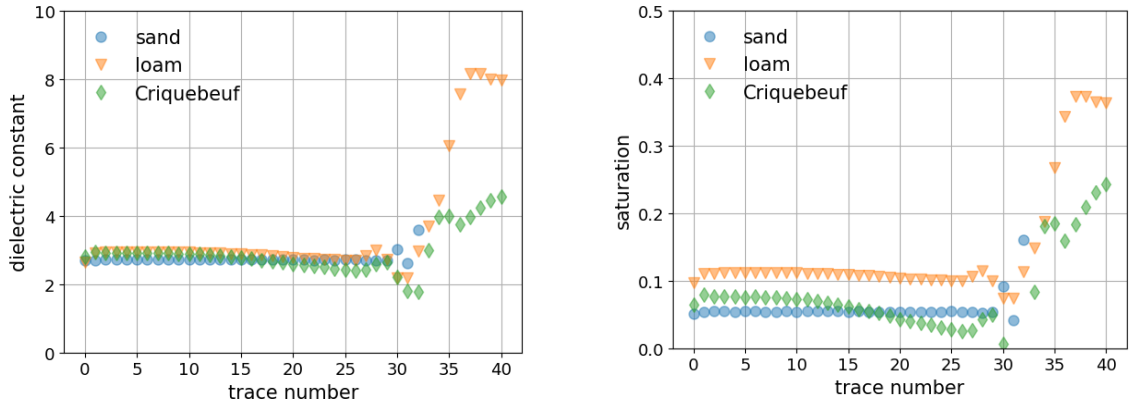

(a) (b)

Figure 10 (a) Dielectric permittivity of the surface soil during the leakage derived from the reflection coefficient. (b) Estimation of the saturation of the surface soils during the leakage based on the dielectric model obtained in Figure 4.

Compared to the water leaks in urban underground pipelines, the size of our physical model is limited, and the effects of the box boundaries cannot be completely eliminated. However, one of the advantages of this setup is that we can use SFR (from 1.6 GHz to 6 GHz) to record the leakage process in different soils with high resolution. The data obtained can help us to understand the influence of water on the evolution of A-scans and B-scans: specifically (i) peak shifts related to the movement of the wet soil front and soil deconsolidation, and (ii) changes in the amplitude of the reflection parameter $|S_{11}|$, which can help us estimate the geometric deformation and saturation of the surface soil during the leakage. These findings can help in understanding the anomalies caused by water leakage in radar applications on a larger scale.

Detecting water leaks in a large scale by GPR

I Description of site and experimental process

The Centre d'Étude et de Recherche (CER) of Cerema Normandie Center constructed two full-scale trenches to observe water leaks. The surface area of the site is 8 x 5 m². The layout, including the positioning of the tubes (PVC, Φ = 100 mm) and the holes created to simulate leaks, is shown in Figure 11. The difference between the two trenches lies in leak's speed: Trench 1 has a tube with three holes, which makes the leak fast, while Trench 2 has a tube with a single hole, which makes the leak slow, as depicted in the schematic.

To simulate long-term leakage in the trench, layers of cardboard and rubber grains (delta gom) were placed beneath the sand layer. The loamy sand layer was compacted layer-by-layer using a machine. When leakage occurs, these two layers become saturated, losing their ability to support the full mass of the trench. As a result, this leads to structural damage in the trench.

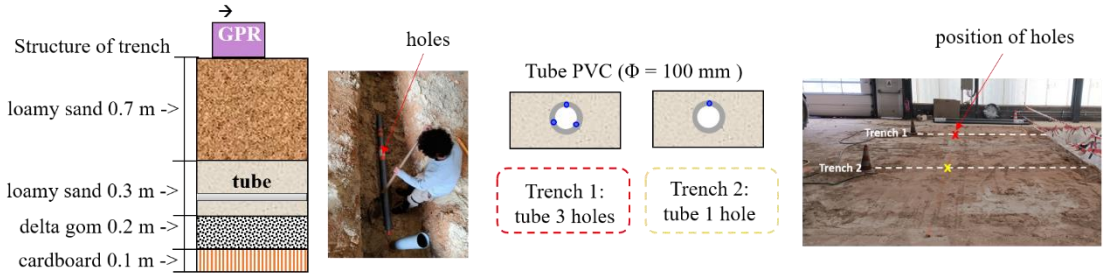

Figure 11 Structure of the two trenches. The red and yellow markers indicate the position of the leak in the two trenches

A commercial ground penetrating radar (GPR, SIR 4000) with a central frequency of 900 MHz was used to detect water leaks in the two trenches. To measure the leakage, we first filled both tubes with water and waited 30 min for stabilization. After that we conducted GPR scans along the tubes. A total of 11 scans were carried out each day, and the observation duration was 5.5 days. The treatment of the B-scans was performed by Open-source Ground Penetrating Radar processing and visualization software [37]. The process involved cutting the start-time between the antenna and soil, filtering the signals by low-cut filter, and background removal. The treated B-scans and the time-domain changes due to the water leaks are shown in Figures 12 and 13.

II Analysis of the trenches with different leak speeds

In Figure 12, according to the actual position of the tubes with holes, the water leaks should be located between 2.3 m and 2.4 m along the distance axis. Along the time axis, the position of the leaks should be below 17 ns considering its real depth. From the series of B-scans obtained in Trench 1 and Trench 2, firstly, we can observe a distinct layer-by-layer structure. This stratification is associated with the compaction during constructing the site, which created a density gradient; Secondly, a quasi-hyperbolic signal at the position of 10 ns and 2 m in Figure 12 (b) is not associated with the tube. After the experiment, we excavated the site and found this signal corresponded to an aggregate of highly compacted wet soil; Thirdly, using the pick program in Reflexw [35], we can track the evolution of the signals related to the water leaks, as indicated by the red and yellow dotted lines in the B-scans.

A comparison of these changes at different leakage durations, as presented in Figure 13 (a) and (b), reveals several trends: in the early stages of the leakage (#01-#02 in Trench 1 and #01-#03 in Trench 2), we observe that the water begins to wet the soil both above and below the tube. However, as the leakage progresses, the water flow continues to fall down in the time axis. There are two possible explanations for this behavior: (i) due to gravity and the relatively low pressure in the tube, the water flow physically fell down in the spatial domain, which in turn increases the travel distance of the EM waves; (ii) the increased dielectric permittivity of the wet soil around the tube in the early stages that slows down the velocity of the signals.

Furthermore, by calculating the ratio between the signals with water leaks and the initial signal, and then identifying the maximum value of this ratio along with the corresponding distance, we can determine the leak position as detected by the GPR, as shown in Figures 13 (c) and (d). A shift in the position of the maximum value is observed, and the extent of this shift is related to both the duration and rate of the leakage. In Trench 1 where the leak speed and volume are relatively large, the detected position moves farther from the initial position as the leakage continues, which decreases the accuracy of detection. In contrast, in Trench 2 where the leak speed and volume are smaller, the shift remains close to the initial hole location throughout the measurements, allowing for more reliable GPR detection. Hence, we conclude that GPR can detect the position of underground water leaks. However, in the case of long-term leaks that saturate the soil, GPR detection becomes less accurate.

Additionally, the presence of a larger leak generated a sinkhole in Trench 1 due to the lack of mechanical resistance from the two layers (cardboard and delta gom) beneath the soil layer, as shown in Figure 14. The position of the sinkhole correlates well with the position of the maximum ratio observed in the final stages (in blue) of Figure 12 (c). Using photogrammetry and Software Metashape, we estimated the depth of the sinkhole to be approximately 20 cm by using an average value of the vertical axis along the two profiles (P1 and P2 in Figure 14). In Trench 2, where the leak flow rate was much slower, no significant sinkhole formed. Therefore, long-term water leakage not only leads to economic waste but also poses a potential hazard to urban safety.

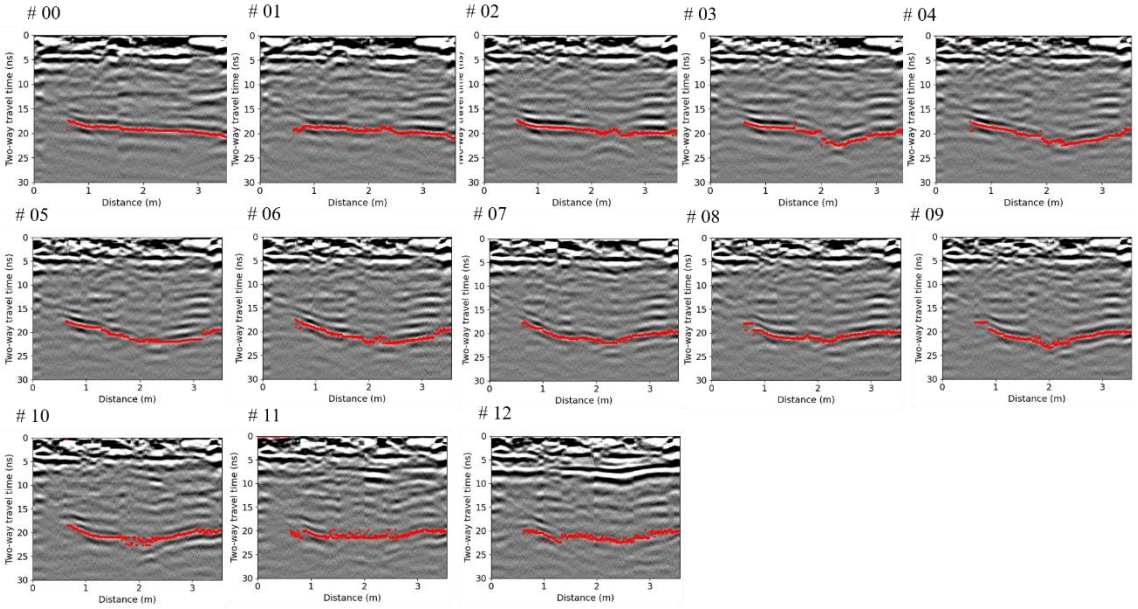

(a)

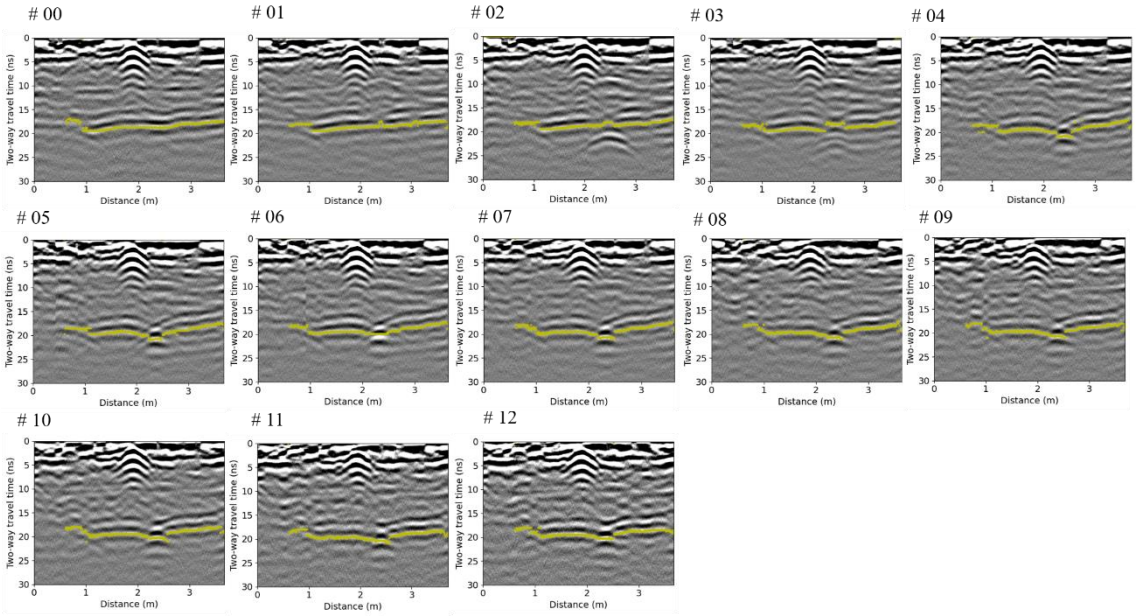

(b)

Figure 12 B-scans during the water leakage (a) for Trench 1 and (b) for Trench 2: The dotted line in each B-scan corresponds to the time shift caused by the water leak. #00 represents the initial state without a leak. The series from #01 to #12 show the changes as the leakage duration increases.

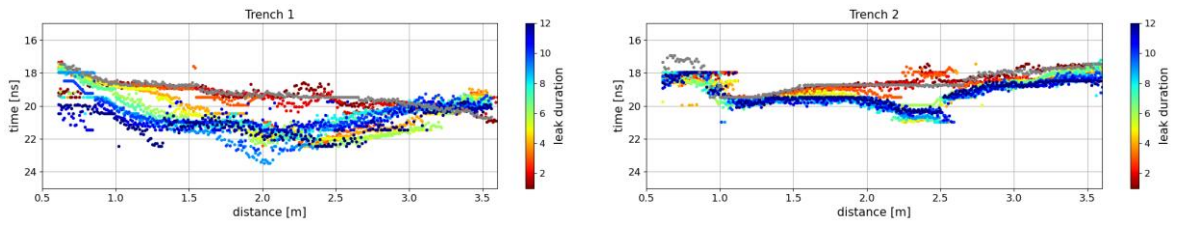

(a) (b)

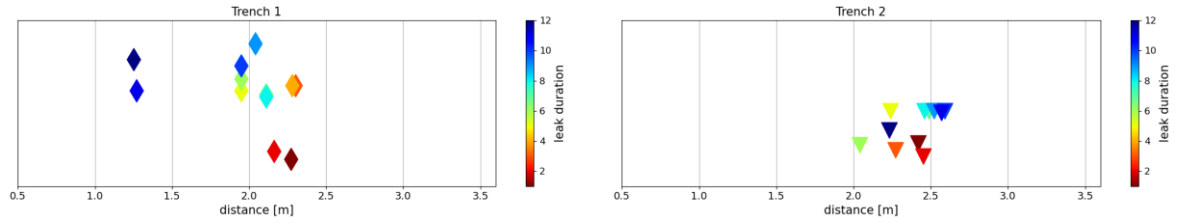

(c) (d)

Figure 13 Comparison of time changes caused by water leaks, (a) for Trench 1 and (b) for Trench 2: The gray line represents the initial state without a leak. The other lines in different colors show the progressive changes in the B-scans as the leakage continues. Maximum value of the ratio of the signals during the leakage to the initial signal, (c) for Trench 1 and (d) for Trench 2.

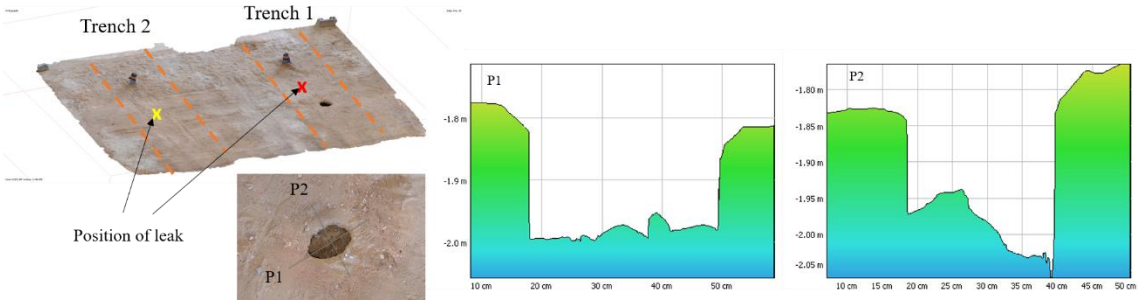

Figure 14 Model of the tested site with two trenches obtained by photogrammetry: the red and yellow markers represent the positions of the holes in the underground tubes. A sinkhole is observed in Trench 1, and its geometry is estimated by two profile (P1 and P2) by Metashape software.

Conclusion

In this study, we demonstrate the potential application of radar for detecting water leaks from underground pipelines at different scales. In the laboratory tests, firstly the dielectric characterization of three types of soils (sand, loam, and Criquebeuf) reveals that the dielectric behaviors depend on soil's properties, such as water saturation, grain size distribution and shape. We have established models that relate the dielectric properties (permittivity and conductivity) to the soil saturation, which can be used to interpret radar signals. In the second phase, using SFR to observe the leakage process in physical models made from these tested soils, we visualized the wet soil front and estimated soil surface deformation and saturation levels. In the field tests, GPR with antenna of 900 MHz was used to detect water leaks in loamy sand at depths of at least 1 m, which is typical for drinking water pipes in the urban environments in France.

The accuracy of the leak detection depends on both the speed and duration of the leak. As the speed and duration increase, the accuracy of radar-based localization decreases. Long-term water leaks pose a risk of structural damage to the soil. We have to admit that in this work the radar method has been applied on the site that we know well. For more general cases, especially the sites that we do not have the map of underground pipelines, then the detection will be much more complicated. Thus, in future we will combine 3D radar and other geophysical tools such as infrared cameras to test more sites with various soil kinds, pipeline geometries and dispersions, to ameliorate the methodology of leak detection. Additionally, to further understand the dielectric properties of the unsaturated soil, the characterization of the mineralogical properties, polycrystalline structures, and micro-morphology of these soils will be carried out in future.

Acknowledgements

This work was funded by "La Fondation d'Entreprise FEREC" in 2023. The authors would like to express their gratitude to the Centre d'Étude et de Recherche (CER) at Cerema Normandie Center for their support in constructing the test site, and to the Master student of Cergy Université, Miss Aminada Sane, for her GPR manipulation in the test site during the internship.

References

[1] Europe's state of water 2024: The need for improved water resilience, EN PDF: TH-AL-24-008-EN-N - ISBN: 978-92-9480-653-6 - ISSN: 1977-8449 - doi: 10.2800/02236

[2] Rodina L, Defining "water resilience": Debates, concepts, approaches, and gaps, WIREs Water, 2019; 6:2, https://doi.org/10.1002/wat2.1334

[3] Guarino P.M., Santo, A., Forte, G. De Falco M., Maria Antonia Niceforo M. Analysis of a database for anthropogenic sinkhole triggering and zonation in the Naples hinterland (Southern Italy). Nat Hazards 2018; 91: 173–192 https://doi.org/10.1007/s11069-017-3054-5

[4] Lei, M., Gao, Y., Jiang, X. Current Status and Strategic Planning of Sinkhole Collapses in China. Eng. Geo. Soc. Terr. Springer. 2015; 5. https://doi.org/10.1007/978-3-319-09048-1_102

[5] Rui L., Huang H., Xin K., Tao T. A review of methods for burst/leakage detection and location in water distribution systems. Water Supply. 2015; 15 (3): 429-441 https://doi.org/10.2166/ws.2014.131

[6] Joseph K., Sharma A.K., Van Staden R., Wasantha P.L.P., Cotton J., Small S. Application of software and hardware-based technologies in leaks and burst detection in water pipe networks: A literature review. Water 2023; 15: 2046. https://doi.org/10.3390/ w15112046

[7] Fan H., Tariq S., Zayed T., Acoustic leak detection approaches for water pipelines, Autom. Constr. 2022; 138: 104226, https://doi.org/10.1016/j.autcon.2022.104226

[8] Santamarina J.C., Park J., Terzariol M., Cardona A., Castro G.M., Cha W., Garcia A., Hakiki F., Lyu C., Salva M., Shen Y., Sun Z., Chong S., Soil properties: Physics Inspired, Data Driven, Springer Nature Switzerland AG 2019

[9] Campbell B A 2002 Radar Remote Sensing of Planetary Surfaces, Cambridge University Press

[10] Hallikainen M. T., Ulaby F. T., Dobson M. C., El-Rayes M. Wu A., L., Microwave dielectric behavior of wet soil-Part 1: Empirical models and experimental observations, IEEE Trans. Geosci. Remote Sens. 1985; GE-23 (1): pp. 25-34. doi: 10.1109/TGRS.1985.289497

[11] Wagner N., Emmerich K., Bonitz F. and Kupfer K., Experimental investigations on the frequency- and temperature-dependent dielectric material properties of Soil, IEEE Trans. Geosci. Remote Sens. 2011; 49 (7): pp. 2518-2530. doi: 10.1109/TGRS.2011.2108303.

[12] Giannakis I., Giannopoulos A. and Warren C. A Realistic FDTD numerical modeling framework of ground penetrating radar for landmine detection, IEEE J. Sel. Top. Appl. Earth Obs. Remote Sens. 2016; 9 (1): pp. 37-51. doi: 10.1109/JSTARS.2015.2468597.

[13] Lai W.W.L.., Dérobert X., Annan P., A review of ground penetrating radar application in civil engineering: A 30-year journey from locating and testing to imaging and diagnosis. NDT&E. Int. 2018; 96: 58-78. https://doi.org/10.1016/j.ndteint.2017.04.002

[14] Lau K.W.P., Cheung B.W.Y., Lai W.W.L., Sham J. F.C, Characterizing pipe leakage with a combination of GPR wave velocity algorithms, Tunn. Undergr. Space Technol. 2021;109: 103740. https://doi.org/10.1016/j.tust.2020.103740

[15] Bai X., Yang Y., Wei, S., Chen G., Li H., Li Y., Tian H., Zhang T., Cui H. A. Comprehensive review of conventional and deep learning approaches for ground-penetrating radar detection of raw data. Appl. Sci. 2023; 13: 7992. https://doi.org/10.3390/app13137992

[16] Carrive P., Saintenoy A., Léger E.; Arcone S.A., Sailhac P. Exploiting ground-penetrating radar signal enhancement by water-saturated bulb surrounding defective waterpipes for leak detection. Geosciences 2022; 12; 368. https://doi.org/10.3390/geosciences12100368

[17] Zhu H., Xiao F., Zhou Y, Lai W.W.L., Zhang Q., A framework for GPR-based water leakage detection by integrating hydromechanical modelling into electromagnetic modelling. Near Surf. Geophys. 2023;1–13, https://doi.org/10.1002/nsg.12281

[18] Hyun S.Y., Jo Y.S., Oh H.C., Kim S.Y. and Kim Y.S. The laboratory scaled-down model of a ground-penetrating radar for leak detection of water pipes. Meas. Sci. Technol. 2007; 18:2791., DOI 10.1088/0957-0233/18/9/008

[19] Lai W. W.L., Chang R. K.W., Sham J. F.C., Pang K. Perturbation mapping of water leak in buried water pipes via laboratory validation experiments with high-frequency ground penetrating radar (GPR), Tunn. Undergr. Space Technol. 2016; 52: 157–167. http://dx.doi.org/10.1016/j.tust.2015.10.017

[20] De Coster A., Pérez Medina J.L., Nottebaere M., Alkhalifeh K., Neyt X., Vanderdonckt J., Lambot S. Towards an improvement of GPR-based detection of pipes and leaks in water distribution networks, J. App. Geophys. 2019; 162: 138–151, https://doi.org/10.1016/j.jappgeo.2019.02.001

[21] Demirci S., Yigit E., Eskidemir I.S., Ozdemir C., Ground penetrating radar imaging of water leaks from buried pipes based on back-projection method. NDT&E. Int. 2012; 47: 35–42. https://doi.org/10.1016/j.ndteint.2011.12.008

[22] Antoine R., Fauchard C., Fargier Y. and Durand E., Detection of leakage areas in an earth embankment from GPR Measurements and permeability logging. Geophys. J. Int. 2015; 610172, http://dx.doi.org/10.1155/2015/610172

[23] Park S., Lim H., Tamang B., Jin J., Lee S., Park S., Kim Y., A Preliminary study on leakage detection of deteriorated underground sewer pipes using aerial thermal imaging. Int. J. Civ. Eng. 2020;18: 1167–1178, https://doi.org/10.1007/s40999-020-00521-8

[24] Gamal M., Di Q., Zhang J., Fu C., Ebrahim S., El-Raouf A.A. Utilizing ground-penetrating radar for water leak detection and pipe material characterization in environmental studies: A case study. Remote Sens. 2023; 15: 4924. https://doi.org/10.3390/rs15204924

[25] Deng S., Ma S., Zhang W. and Zhang S., Integrated detection of a complex underground water supply pipeline system in an old urban community in China, Sustainability 2020; 12: 1670. doi:10.3390/su12041670

[26] Norme NF EN 933-9 : Essais pour déterminer les caractéristiques géométriques des granulats – Partie 9 : Qualification des fines — Essai au bleu de méthylène, Paris, Association Française de Normalisation (AFNOR), 1999, 16

[27] Fan B., Bosc F., Liu Y., Fauchard C., Dielectric measurement by open-ended coaxial line for hot-mix asphalt roads: From laboratory test to on-site investigation, NDT & E Int. 2023; 138: 102872, https://doi.org/10.1016/j.ndteint.2023.102872

[28] Filali B., Boone F., Rhazi J., Ballivy G. Design and calibration of a large open-ended coaxial probe for the measurement of the dielectric properties of concrete. IEEE Trans. Microw. Theory Techn. 2008; 10: 2322 - 2328. doi: 10.1109/TMTT.2008.2003520

[29] Guihard V., Taillade F., Balayssac J., Steck B., Sanahuja J., Deby F. Permittivity measurement of cementitious materials with an open-ended coaxial probe. Constr. Build. Mater. 2020; 230: 116946. doi: 10.1016/j.conbuildmat.2019.116946

[30] Otto G.P. and Chew W.C. Improved Calibration of a large open-ended coaxial probe for dielectric measurements. IEEE Trans. Instrum. Meas. 1991; 40: 742 – 746. doi: 10.1109/19.85345

[31] Kaatze U. Measuring the dielectric properties of materials. Ninety-year development from low-frequency techniques to broadband spectroscopy and high-frequency imaging. Meas Sci Technol. 2013; 24. 012005. doi: 10.1088/0957-0233/24/1/012005

[32] Revil A. Effective conductivity and permittivity of unsaturated porous materials in the frequency range 1 mHz -1 GHz, Water Resour. Res. 2013; 49: 306-327. https://doi.org/10.1029/2012WR012700

[33] Topp G. C., Davis J. L., Annan A. P., Electromagnetic determination of soil water content: Measurements in coaxial transmission lines, Water Resour. Res. 1980; 16(3): 574-582, https://doi.org/10.1029/WR016i003p00574

[34] Birchak J. R., Gardner C. G., Hipp J. E. and Victor J. M. High dielectric constant microwave probes for sensing soil moisture. Proc. IEEE. 1974; 62 (1): pp. 93-98. doi: 10.1109/PROC.1974.9388.

[35] REFLEX 3.0 manual, Sandmeier geophysical software, 2008

[36] Araujo S., Beaucamp B., Delbreilh L., Dargent E., Fauchard C., Compactness/density assessment of newly-paved highway containing recycled asphalt pavement by means of non-nuclear method, Constr. Build. Mater. 2017; 154. https://doi.org/10.1016/j.conbuildmat.2017.07.075

[37] Plattner A. M., GPRPy: Open-source ground-penetrating radar processing and visualization software," The Leading Edge. 2020; 39: 332–337. https://doi.org/10.1190/tle39050332.1